Pure Appl. Geophys. 178 (2021), 3441–3460

https://doi.org/10.1007/s00024-021-02814-y

Pure and Applied Geophysics

Inter-Source Interferometry of Seismic Body Waves: Required Conditions and Examples

Patipan Saengduean,[1] Morgan P. Moschetti,[2] and Roel Snieder[1]

Abstract—Seismic interferometry is widely applied to retrieve wavefields propagating between receivers. Another version of seismic interferometry, called inter-source interferometry, uses the principles of seismic reciprocity and expands interferometric applications to retrieve waves that propagate between two seismic sources. Previous studies of inter-source interferometry usually involve surface-wave and coda-wave estimations. We use inter-source interferometry to estimate the P-waves propagating between two sources rather than the estimation of surface waves and coda waves. We show that the recovered arrival times are dependent on the accuracy of the earthquake catalog of the two sources. Using inter-source interferometry, one can recover the waveform of the direct body waves and potentially reconstruct the waveform of coda waves, depending on the source-receiver geometry. The retrieval of these waveforms is accurate only when the wavefield is sampled with approximately 4 receivers per wavelength in the stationary phase zone. We show that using only receivers inside the stationary phase region for inter-source interferometry introduces the phase error of approximately 0.3 radians. In our study, we show an example of the P-wavefield reconstruction between two earthquakes using the seismic records from an array along San Andreas Fault. The retrieved P waves give a qualitative estimation of the thickness of the low-velocity zone of San Andreas Fault of approximately 4 km.

Keywords: Seismic interferometry, inter-source interferometry, Fresnel integral, body waves, fault zone, San Andreas Fault.

1. Introduction

Seismic interferometry is a technique to estimate the Green's function or the wavefield that accounts for wave propagation between receivers. The inter-receiver technique has been developed for many applications using ambient noise (Shapiro et al. 2005; Draganov et al. 2007), traffic and oilfield production noise (Nakata et al. 2011; Miyazawa et al. 2008), and earthquakes or active sources. The principles of seismic interferometry are explained in several review papers (Curtis et al. 2006; Larose et al. 2006; Wapenaar et al. 2010; Snieder and Larose 2013).

In general, one can retrieve the Green's function between receivers using cross-correlation, deconvolution, and cross-coherence of the signals recorded at receivers (Snieder et al. 2009; Nakata et al. 2011). Although applications of seismic interferometry are usually based on cross-correlation (Shapiro et al. 2005; Miyazawa et al. 2008; Mordret et al. 2010; Asano et al. 2017), some applications also use deconvolution (Vasconcelos and Snieder 2008b, a; Nakata et al. 2013; van Dalen et al. 2015; Pianese et al. 2018), cross-coherence (Prieto et al. 2009; Nakata et al. 2011), and convolution (Curtis and Halliday 2010; Entwistle et al. 2015). These data processing methods for Green's function retrieval have diverse advantages and disadvantages (Snieder et al. 2009). One has to select the process that is best suited to particular data and research requirements. In theory, cross-correlation of ambient seismic noise interferometry suppresses strong amplitudes of earthquakes. In this study, we implement cross-correlation for Green's function retrieval because, unlike in the case of noise interferometry, we use real earthquakes, and the cross-correlation correctly handles the strong amplitudes of the waves that are excited by these earthquakes.

Recovering the Green's function using inter-receiver interferometry, in particular with the retrieval of surface waves from ambient noise cross-correlation, has become an accepted technique (Shapiro et al. 2005). For practical reasons, the receivers used are usually installed on the Earth's surface. A version of seismic interferometry, called inter-source

[1] Center for Wave Phenomena, Colorado School of Mines, Golden, CO, USA. E-mail: psaengduean@mymail.mines.edu; rsnieder@mines.edu

[2] U.S. Geological Survey, Denver, CO, USA. E-mail: mmoschetti@usgs.gov

interferometry (Curtis et al. 2009), addresses this limitation because it yields the waves that propagate between two sources, which may be located in the subsurface.

Inter-source interferometry, or the virtual receiver method (VRM), is a technique to estimate the Green's function that accounts for wave propagation between two earthquakes, one of which acts as a virtual receiver. The Green's function retrieved from the inter-source technique is the wavefield measured through the dynamic strain induced by the wavefield at one of the earthquakes excited by the other earthquake (Curtis et al. 2009). Even though the theory of inter-source interferometry for Green's function retrieval requires receivers on a closed surface surrounding the earthquakes, the dominant contribution of the retrieved Green's function comes from the receivers located inside the stationary phase zones of the pair of sources (Snieder 2004; Curtis et al. 2009).

Inter-source interferometry as introduced by Curtis et al. (2009) has been applied in several studies. One application involves the monitoring of micro-seismic events by observing the change in the source mechanism inversion of the Green's function retrieved from these events (Matzel et al. 2016; Morency and Matzel 2017). Other applications of inter-source interferometry include the improvement of crustal structure tomography using inter-event interferometry (Shirzad et al. 2019), the localization and identification of the geometry of the metastable olivine wedge (Shen and Zhan 2020), and the determination of the shear-wave velocity in different source clusters (Eulenfeld 2020). In addition, Schuster (2009) uses interferometry to convert VSP data into surface seismic data and thus extracts the waves that propagate between active sources at the surface. Curtis and Halliday (2010) use inter-source interferometry as a part of a new form of interferometry called source-receiver interferometry. Poliannikov et al. (2012) image a subduction slab using virtual responses between earthquakes located inside the slab. Liu et al. (2016) turn non-transient sources such as drill-bit noise into virtual receivers, imaging the redatumed reflection responses close to targeted areas.

Previous studies of inter-source interferometry usually estimate the Green's function using the cross-correlation of surface waves, measuring the dispersion of the waves. However, the estimation of body waves using seismic interferometry involves stricter requirements on the source-receiver geometry than the extraction of surface waves (Forghani and Snieder 2010; Nakata et al. 2011). Since inter-source interferometry can yield the waves that propagate between earthquakes, this technique has the potential to extract the body waves that propagate between these earthquakes.

In order to construct the Green's function using seismic interferometry, one has to satisfy the theoretical requirements on the source or reciever distribution. Fan and Snieder (2009) have derived sampling criteria for inter-receiver interferometry. Due to seismic reciprocity, which allows for the exchange of the source and receiver positions, the same criteria holds for the inter-source technique. However, noise sources in the inter-receiver interferometry tend to have better spatial distribution than that of receivers in inter-source interferometry (Fig. 1a and d). At the global scale, dominant noise sources (e.g., oceanic waves) are omnipresent, while smaller-scale noise sources (e.g., traffic and cultural noises) are concentrated at particular locations such as roads and construction sites. In inter-source interferometry, the reconstruction quality of the retrieved waves depends on the spatial distribution of surface receivers. Thus, the applicability of inter-source interferometry depends on the geometry of the used receiver array (Fig. 1d).

Instead of measuring the arrival time and the dispersion of surface waves, we seek to retrieve body waves that can be characterized by the following information: (1) the arrival time of the direct wave, (2) the waveform of the direct wave, and (3) the waveform of coda waves. In our study, we test to what extent we can recover this information; we also identify the required sampling criteria (i.e., sampling density and station locations) for the retrieval of this information using inter-source interferometry. We present the Green's function retrieval from the cross-correlation of (1) 2D synthetic acoustic waves excited from two sources in a homogeneous medium with an embedded scatterer and (2) earthquake seismograms recorded at an array deployed along San Andreas

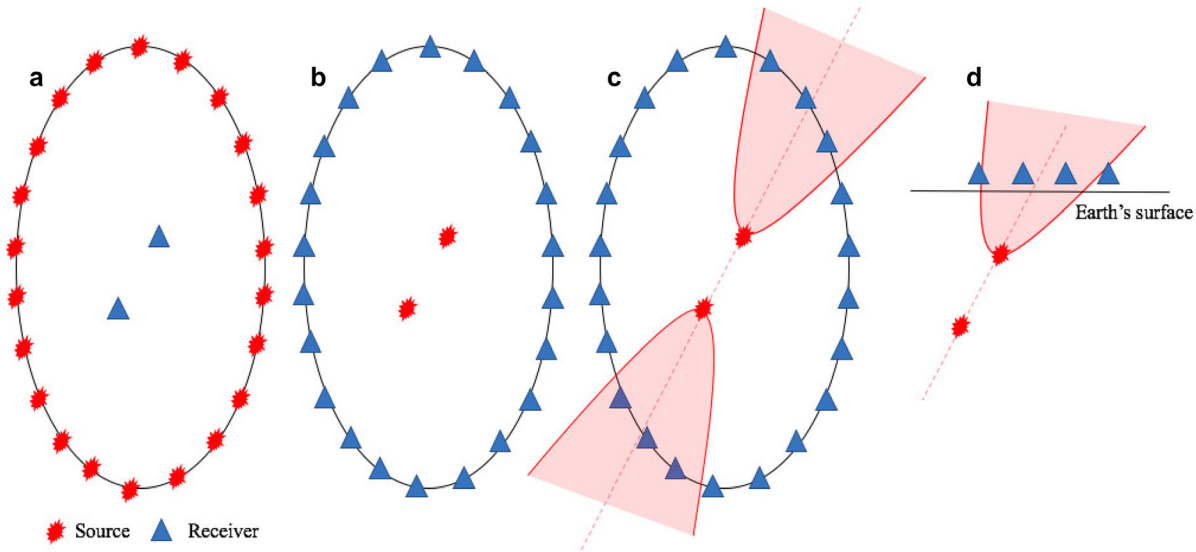

Figure 1
Cartoon of **a** inter-receiver interferometry with noise or active sources on a closed surface, **b** inter-source interferometry with receivers on a closed surface, **c** inter-source interferometry with receivers in stationary phase zones (pink areas), and **d** inter-source interferometry with surface receivers in one stationary phase zone

Fault. The retrieval uses inter-source interferometry and receivers located in the stationary phase zones.

We first introduce the basic equations of cross-correlation based interferometry and the data processing steps. We further demonstrate the Green's function retrieval using different stationary phase zones and sampling density for the synthetic model. Next, we show a field example of Green's function reconstruction of P waves and the qualitative estimation of the low-velocity zone thickness of the San Andreas Fault (SAF) using the reconstructed P waves. Finally, we explain the reason why we can recover parts of the waveform, yet cannot recover the arrival time and the full waveform of body waves using inter-source interferometry; we also discuss the application of the inter-source technique with field examples.

2. *Theory of Cross-Correlation Based Interferometry*

Using the Fourier convention $f(t) = \int F(\omega)e^{i\omega t}d\omega$ and assuming a far-field integration boundary oriented perpendicularly to wave propagation, Wapenaar and Fokkema (2006) have derived seismic interferometry for acoustic waves:

$$G(\mathbf{x}_A, \mathbf{x}_B, \omega) - G^*(\mathbf{x}_A, \mathbf{x}_B, \omega) \approx -\frac{2i\omega}{\rho c}\oint G(\mathbf{x}_B, \mathbf{x}, \omega)G^*(\mathbf{x}_A, \mathbf{x}, \omega)d^2\mathbf{x}, \quad (1)$$

where $G(\mathbf{x}_A, \mathbf{x}_B, \omega)$ is the frequency-domain representation of the Green's function that accounts for the wave propagation from $\mathbf{x}_B$ to $\mathbf{x}_A$, ρ is the mass density, c is the wave velocity, ω is the angular frequency, and the asterisk denotes the complex conjugation. The factor $i\omega$ corresponds to a differentiation in the time domain.

In the frequency domain, the wavefield $u(\mathbf{x}_A, \mathbf{x}, \omega)$ excited from a point source at $\mathbf{x}$ and recorded at $\mathbf{x}_A$ is the Green's function $G(\mathbf{x}_A, \mathbf{x}, \omega)$ convolved with the source-time function $W(\mathbf{x}, \omega)$. The cross-correlation of the wavefields measured at $\mathbf{x}_A$ and $\mathbf{x}_B$ is, in the frequency domain, given by

$$C_{BA} = u(\mathbf{x}_B, \mathbf{x}, \omega)u^*(\mathbf{x}_A, \mathbf{x}, \omega) = |W(\mathbf{x}, \omega)|^2 G(\mathbf{x}_B, \mathbf{x}, \omega)G^*(\mathbf{x}_A, \mathbf{x}, \omega). \quad (2)$$

Integrating the cross-correlation in Eq. (2) over a closed surface that includes uncorrelated sources on

the closed surface surrounding the receivers (Snieder et al. 2007) gives

$$\oint C_{BA} d^2\mathbf{x} = \langle |W(\mathbf{x},\omega)|^2 \rangle \oint G(\mathbf{x}_B,\mathbf{x},\omega) G^*(\mathbf{x}_A,\mathbf{x},\omega) d^2\mathbf{x}, \tag{3}$$

where $\langle |W(\mathbf{x},\omega)|^2 \rangle$ is the average of the spectrum of the squared source-time functions. In practice, we carry out the integration by stacking all sources on the closed surface (Fig. 1a). Inserting the integration of cross-correlation of Eq. (3) into Eq. (1) yields:

$$\left[G(\mathbf{x}_A,\mathbf{x}_B,\omega) - G^*(\mathbf{x}_A,\mathbf{x}_B,\omega)\right] \langle |W(\mathbf{x},\omega)|^2 \rangle \approx -\frac{2i\omega}{\rho c} \oint C_{BA} d^2\mathbf{x}, \tag{4}$$

where $G(\mathbf{x}_A,\mathbf{x}_B,\omega) - G^*(\mathbf{x}_A,\mathbf{x}_B,\omega)$ denotes the difference of the causal and acausal parts of the Green's function that accounts for wave propagation between receivers at $\mathbf{x}_A$ and $\mathbf{x}_B$. Equations (1)–(4) represent the theory of cross-correlation based inter-receiver interferometry. With source-receiver reciprocity, the equations also hold for inter-source interferometry as Curtis et al. (2009) show that one can estimate the same Green's function that accounts for the wave propagation between two sources at the same $\mathbf{x}_A$ and $\mathbf{x}_B$ locations, using the records at receivers on a closed surface (Fig. 1b) or surface receivers located in the stationary phase zone (Fig. 1c and 1d). In our study, we define the width of the stationary phase zone as the region where the phase change of the interferometric integral compared to the point where the phase is at an extremum is a specified fraction of the dominant period. In our study, we use a quarter of the dominant period (Appendix A). The width of the phase zone depends on the source-receiver geometry and is explained in the following sections.

As shown by Curtis et al. (2009), inter-source interferometry for moment tensor sources $\mathbf{M}^A$ and $\mathbf{M}^B$ at locations $\mathbf{x}^A$ and $\mathbf{x}^B$, respectively, gives an interferometric measurement

$$v = M^B_{ip} M^A_{mq} \partial^B_p \partial^A_q G_{im}(\mathbf{x}^B,\mathbf{x}^A)\ . \tag{5}$$

As shown by Aki and Richards (2002), the displacement generated by a moment tensor source $\mathbf{M}^A$ at $\mathbf{x}^A$ is given by

$$u_i^{mom}(\mathbf{x}) = M^A_{mq} \partial^A_q G_{im}(\mathbf{x}^B,\mathbf{x}^A), \tag{6}$$

where G denotes the elastic wave Green's tensor. According to expression (5), inter-source interferometry thus extracts

$$v = M^B_{ip} \partial^B_p u_i^{mom}(\mathbf{x}^B). \tag{7}$$

Since the moment tensor M^B_{ip} is symmetric, this can also be written as

$$v = M^B_{ip} \varepsilon^{mom}_{pi}(\mathbf{x}^B), \tag{8}$$

where $\varepsilon^{mom}_{pi} = (1/2)\left(\partial_p u_i^{mom} + \partial_i u_p^{mom}\right)$ is the strain field. This means that inter-source interferometry gives the projection of the strain field at $\mathbf{x}^B$ onto the moment tensor $\mathbf{M}^B$ that is associated with elastic waves excited by a moment tensor source $\mathbf{M}^A$ at location $\mathbf{x}^A$.

3. Synthetic Model and Green's Function Retrieval

In a 2D synthetic example, we compute acoustic wavefields in a homogeneous model with a single embedded scatterer. As shown in Fig. 2, two seismic sources are located at depths of 3 km and 7 km with a horizontal separation of 3 km. The scatterer is located at a depth of 7 km with a horizontal separation of 3 and 6 km from the two sources, respectively. In our model, 801 receivers are located on the surface with a

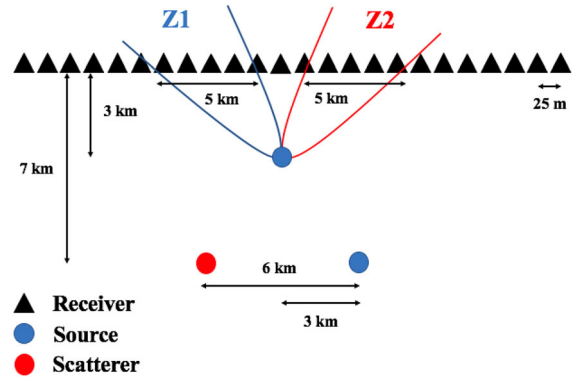

Figure 2
Cartoon of 2D synthetic model used to compute acoustic wavefields. The model includes two sources and a scatterer. The stationary phase zones for the direct and scattered waves propagated between the two sources are Z1 and Z2, respectively. The receiver separation is 25 m and is not drawn to scale

uniform separation distance of 25 m between receivers. The wave velocity of this medium is 4 km/s and the frequency range is 1–10 Hz; thus, the shortest wavelength of this model is 400 m. Figure 2 is a sketch of our synthetic model with two 5 km-wide stationary phase zones; Z1 and Z2 represent the zones for the direct wave between two earthquakes and the scattered wave from the scatterer, respectively.

We use the cross-correlation based method to construct the Green's function between two seismic sources. We first compute the cross-correlation of full wavefields excited from the two sources that are recorded at all receivers located in the two stationary phase zones. Next, we apply a Gaussian taper to the cross-correlated traces at the receivers before computing the integration of cross-correlations; the tapering minimizes the truncation artifacts resulting from the truncation of the integration interval (Burdick and Orcutt 1979). The tapering employs a Gaussian window, $w(x) = e^{-(x-x_0)^2/2\sigma^2}$, where x is the receiver location away from the center of the stationary phase zone (x_0) and σ is 40% of the width of the receivers array located within the stationary phase region. For a meaningful comparison, we use Eq. (4) to match the integrated correlogram with the direct forward-modelled wavefield between the two sources convolved with the source-time function. To recover the Green's function, one needs to take the time derivative of the integrated correlogram and deconvolve with the squared source-time function. In order to avoid a deconvolution, we follow Eq. (4) and compare the scaled time derivative of the correlation (the right hand side of Eq. (4)) with the Green's function's convolved with the power spectrum of the source-time functions (the left hand side of Eq. (4)). Because our comparison uses normalized waveform, we do not account for the constants 2, mass density, and wave velocity in Eq. (4).

The ability to accurately reconstruct the Green's function depends on (1) the location of the receiver array and (2) the sampling density of the array. We test the ability to reconstruct the Green's function using inter-source interferometry, given these two requirements. We first show the comparison between the forward-modeled and the interferometric wavefields when we use all 801 receivers on the surface for inter-source interferometry. Using all the receivers, the waveform extraction is accurate, except for an early arrival at 0.25 s (Fig. 3). This early arrival at 0.25 s with an amplitude of approximately 2.5% of the direct arrival is the contribution from the cross-correlation of scattered waves and has the same arrival time for all receivers (Fig. 4). Snieder et al. (2008) show that a full aperture of receiver array can eliminate the early arrival at 0.25 s. Since we use a limited aperture with receivers only at the surface, we cannot completely eliminate this early arrival.

As the wavefield reconstructed by inter-source interferometry depends on the receiver array location, we test Green's function retrieval using cross-correlation of the wavefields recorded at receivers located in different stationary phase zones. Figures 5 and 6 compare the forward-modeled wavefield and the interferometric Green's function retrieved using only receivers in the stationary phase locations, Z1 and Z2, respectively. Figure 5 illustrates that we can only retrieve the direct wave when we use receivers in the stationary phase zone (Z1) of the direct wave. By contrast, Fig. 6 shows the same comparison, using stations located in the stationary phase zone (Z2) of the scattered wave, indicating that in this case, we can only retrieve the scattered wave. Notice from Figs. 5 and 6 that the limited aperture of the used receiver array located inside the stationary phase zone leads to

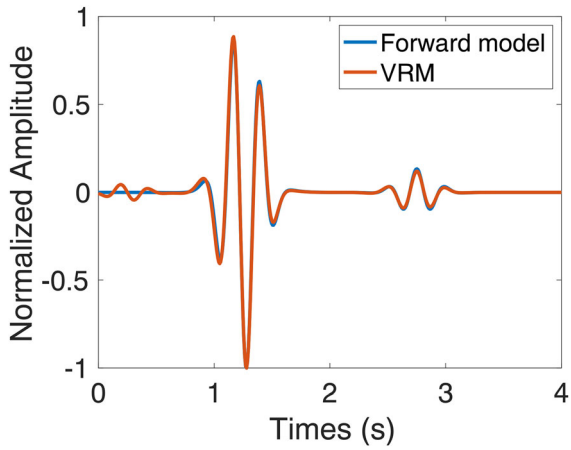

Figure 3
Comparison between the forward-modeled wavefield convolved with the source wavelet (blue) and the Green's function retrieved from the inter-source technique (VRM) with a time derivative correction (red), using all 801 receivers. The amplitude of the two traces are normalized

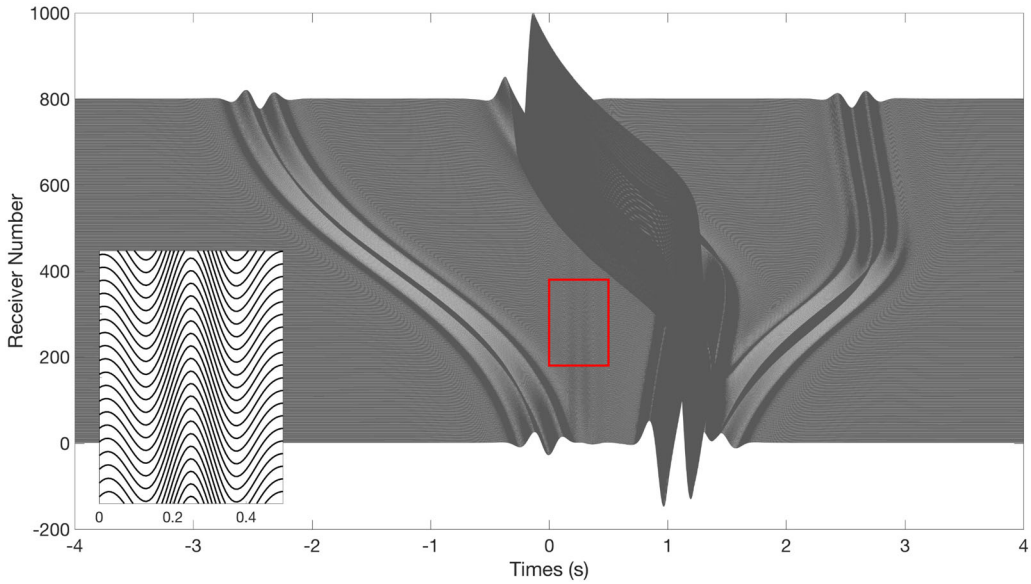

Figure 4
Cross-correlation of wavefields recorded at each individual receiver. The bottom-left plot magnifies the area in the red rectangle, showing weak waves that arrive consistently at 0.25 s at all receivers

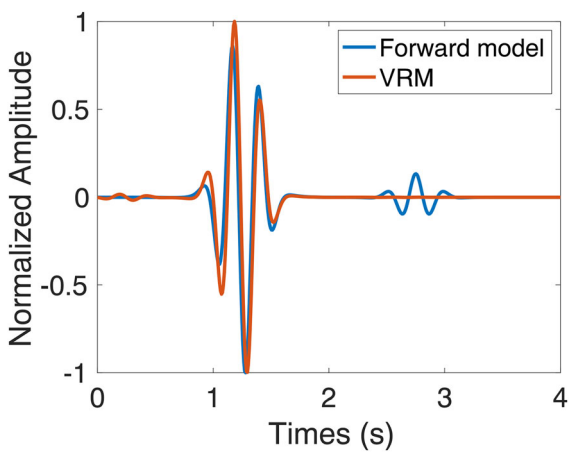

Figure 5
Comparison between the forward-modeled wavefield convolved with the source wavelet (blue) and the Green's function retrieved from the inter-source technique (VRM) with a time derivative correction (red), using receivers located in stationary phase region for inter-source path (Z1). The amplitudes of the traces are normalized

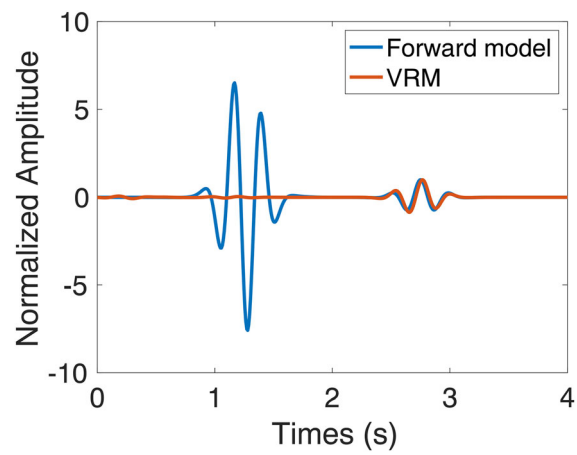

Figure 6
Comparison between the forward-modeled wavefield convolved with the source wavelet (blue) and the Green's function retrieved from the inter-source technique (VRM) with a time derivative correction (red), using receivers located in stationary phase zone for source-scatterer path (Z2). The amplitudes of the two traces are normalized using the amplitude of the scattered wave

a small phase distortion between the forward-modelled and interferometric wavefields.

We show in Appendix A that the small phase distortion in Fig. 5 is due to an integration over receivers that is limited to the stationary phase zone. We also show in the appendix that the stationary phase integral converges slowly in the sense that one needs to integrate over an interval that is much larger than the width of the stationary phase zone as defined earlier, and that an integration over the stationary

phase zone—defined as the region where the maximum phase delay is a quarter of a period—leads to a phase error of about 0.273 radians. This phase error does not depend on the distance between the sources.

In addition to the different receiver array locations, we also test the connection between the sampling density of the station array and the retrieved Green's function using inter-source interferometry by lowering the number of stations and thereby increasing the station spacing inside the two stationary phase zones (Z1 and Z2). The comparison of the forward-modeled and the retrieved traces in Fig. 7 involves stations located in the two stationary phase zones (Z1 and Z2). Using 41 stations with a uniform station spacing of 100 m in each zone, we can recover both the direct and the scattered waves (Fig. 7a). By contrast, Fig. 7b shows the retrieved direct and scattered waves with oscillations prior to the arrival of these waves, using 5 stations in each zone with a uniform station spacing of 1 km. The direct and scattered waves in Fig. 7 are well-reconstructed using the different station spacing because the width of the stationary phase locations is well-covered. In the case of Fig. 7b, the retrieved signal is under-sampled away from the stationary phase regions as the station spacing is much larger than the smallest wavelength of this synthetic model (400 m). Thus, the oscillations prior to the direct and scattered waves are not completely eliminated, compared to the retrieved signal in Fig. 7a. Similar to Figs. 5 and 6, Fig. 7 shows a phase distortion between the forward-modelled and interferometric wavefields due to the limited aperture of the used receiver array located inside the stationary phase zones. We explain the detail of the phase shift in Appendix A. One can mitigate this phase distortion using all receivers on the surface (Fig. 3), but this is usually not possible with realistic surface array.

In this section, we showed that one can reconstruct the waveform of direct body waves, which accounts for the wave propagation between two sources, using inter-source interferomety and seismic records of receivers located in the stationary phase zones. The reconstruction is accurate only when the wavefield is sampled with sufficient spatial sampling

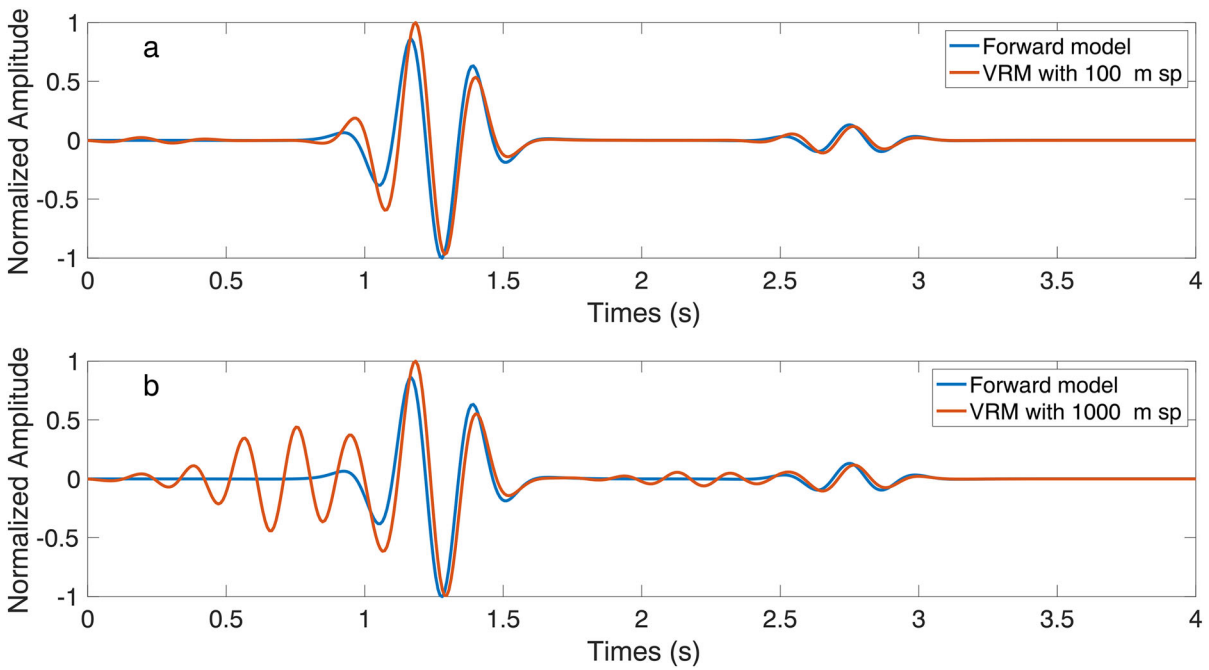

Figure 7
Comparison between the forward-modeled wavefield convolved with the source wavelet (blue) and the Green's function retrieved from the inter-source technique (VRM) with a time derivative correction (red), using receivers located in Z1 and Z2. The amplitude of the two traces are normalized. 7a and 7b have uniform receiver spacings of 100 and 1000 m, respectively, in the stationary phase zones

density. For the direct summation of the cross-correlated wavefields over field array receivers, one requires 4 sampling points in a wavelength because two sampling points are not adequate to numerically integrate an oscillatory function when using a summation over the sampling points; as shown in the top function in Fig. 8, these sampling points of an integrated oscillatory function might be located at zero crossings of the integrand and would thus erroneously suggest that the function vanishes. However, using techniques such as interpolations of the integrand prior to the summation of the integrand (Entwistle et al. 2015) or Filon-Trapizoidal rule for numerically integrating oscillatory integral functions (Tuck 1967), one can reduce the number of required sampling points and only needs more than 2 sampling points in a wavelength. With only the direct integration of the cross-correlations over receivers, one needs at least 4 points per wavelength to numerically integrate such an oscillatory function, although even in that case the numerical quadrature might not be very accurate.

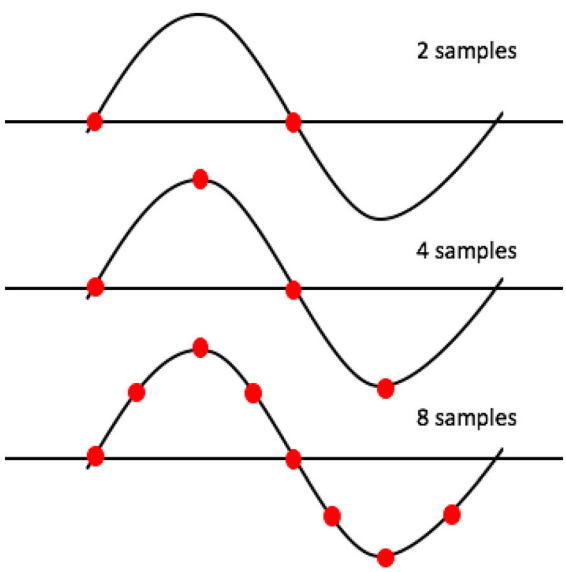

Figure 8
Different numbers of spatial samples for an integrated oscillatory function

4. Green's Function Retrieval Using Seismograms Recorded near the San Andreas Fault (SAF)

Section 3 shows that for the direct summation of the cross-correlated wavefields over array receivers, one requires at least 4 receivers located within the stationary phase locations to reconstruct the waveform of the direct body waves. Here, we exemplify the recovery of direct body waves using the inter-source method and seismic records from two earthquakes recorded at a seismic array inside the stationary phase locations of the two earthquakes.

We select two earthquakes from the U.S. Geological Survey comprehensive earthquake catalog (Guy et al. 2015). The first earthquake ($M_d = 1.48$) occurred on July 11, 2014 at 6:56am with depth of approximately 1 ± 1.4 km. The second earthquake ($M_d = 2.47$) occurred on July 11, 2014 at 12:14 pm with depth of approximately 4 ± 0.2 km. We use the seismograms of the two earthquakes recorded at an array installed in Peachtree Valley, San Andreas Fault (SAF). The array consists of 116 ZLand nodes, along 3 line arrays (Fig. 9). For the interferometry, we use the seismic records of the two local earthquakes from the line array along the SAF (Line 3); seismograms of the earthquakes start at the origin times of the earthquakes from the catalog (Fig. 10). The seismograms are bandpassed between 1 and 3 Hz to accommodate the station spacing of the array and the sampling criteria.

In this study, we perform inter-source interferometry using the waves arriving in the P-wave time windows. We first manually pick the arrival times of P and S waves from the shallow earthquake of each station. Then, we visually pick the P-wave arrival time of the deeper earthquake and determine the local P-wave velocity from the picked P-wave arrivals; assuming straight ray paths between the sources and the surface receivers and using the moveout along the array (local P-wave velocity approximately 4.8 km/s). We assume that the wave-velocity ratio V_p/V_S is constant. Thus, we can estimate the arrival times of S waves for the deeper earthquake and separate the P- and S-wave time windows of the two earthquakes. The windows we use in our interferometric study are from the origin times of the earthquakes up to the S-wave arrivals. We then apply a Hanning taper of 2

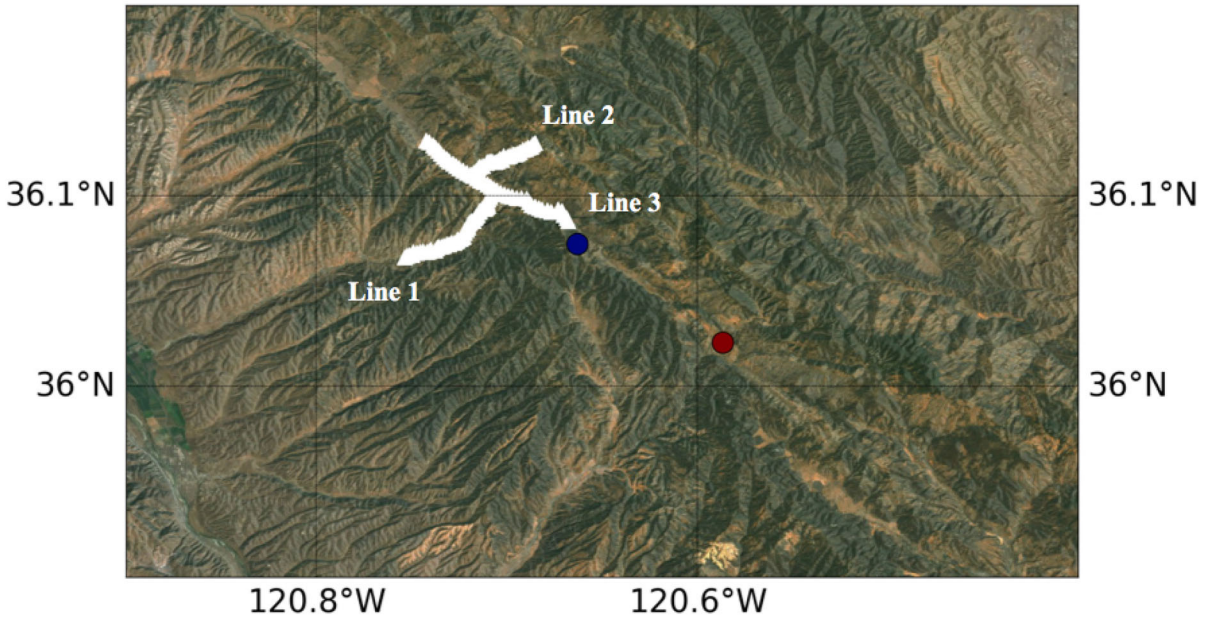

Figure 9
Map view of seismic line arrays (white triangles) along and across San Andreas Fault and earthquakes (circles). Blue and red circles represent the shallow and deeper earthquakes, respectively

periods on both ends of the P-wave signals. Here, all of the seismic stations of the SAF data set are visually located in the stationary phase zone of the two selected earthquakes (Fig. 11). The station spacing of approximately 200 m is less than a quarter of the wavelength for the highest-frequency waves in the selected 1–3 Hz bandpass ($\lambda/4$ is approximately 400 m). The station spacing of the SAF data set thus satisfies the sampling requirement. Since the data at stations 5 and 40 are missing, we cross-correlate the waves in the tapered P-wave windows for stations 6–39 (Fig. 10). Next, we stack the tapered P-wave windows and then taper the sum of the windows, using the Gaussian taper that accounts for approximately 40% of the width of the receivers array used. The two tapers minimize the truncation effects (Burdick and Orcutt 1979). The final process is to take the time derivative of the stacked tapered cross-correlated P-waves. Assuming step functions for the source-time function and using the P-wave seismic records, this provides an estimate of the P-waves that propagate between the two selected earthquakes (Fig. 12a).

Using receivers only along a line, the interferometric P-waves (Fig. 12a) provide a qualitative estimation of the P-wave propagation between the two sources. The interferometric signal in Fig. 12a consists of (1) a direct arrival at approximately 2.5–3 s and (2) a later arrival after approximately 3 s. The timing of the direct arrival is consistent with the expected arrival time determined from the earthquake catalog and the local P-wave velocity of the area.

We recognize the large uncertainty in the depth of the selected earthquakes from the catalog, and this high uncertainty may contribute to the error of the wave retrieval using inter-source interferometry because when the depth of the earthquakes is significantly different from the depths in the catalog, the receiver array may not adequately sample the stationary phase zone of the interferometric integral. To test the effect of the depth sensitivity on the interferometric P-wave retrieval, we use a synthetic homogeneous model with two sources at the same locations of the two selected SAF earthquakes and surface receivers, including the Line 3 (L3) array of 200 m station spacing (Fig. 13a). Figure 13b shows that although the L3 array does not cover the whole

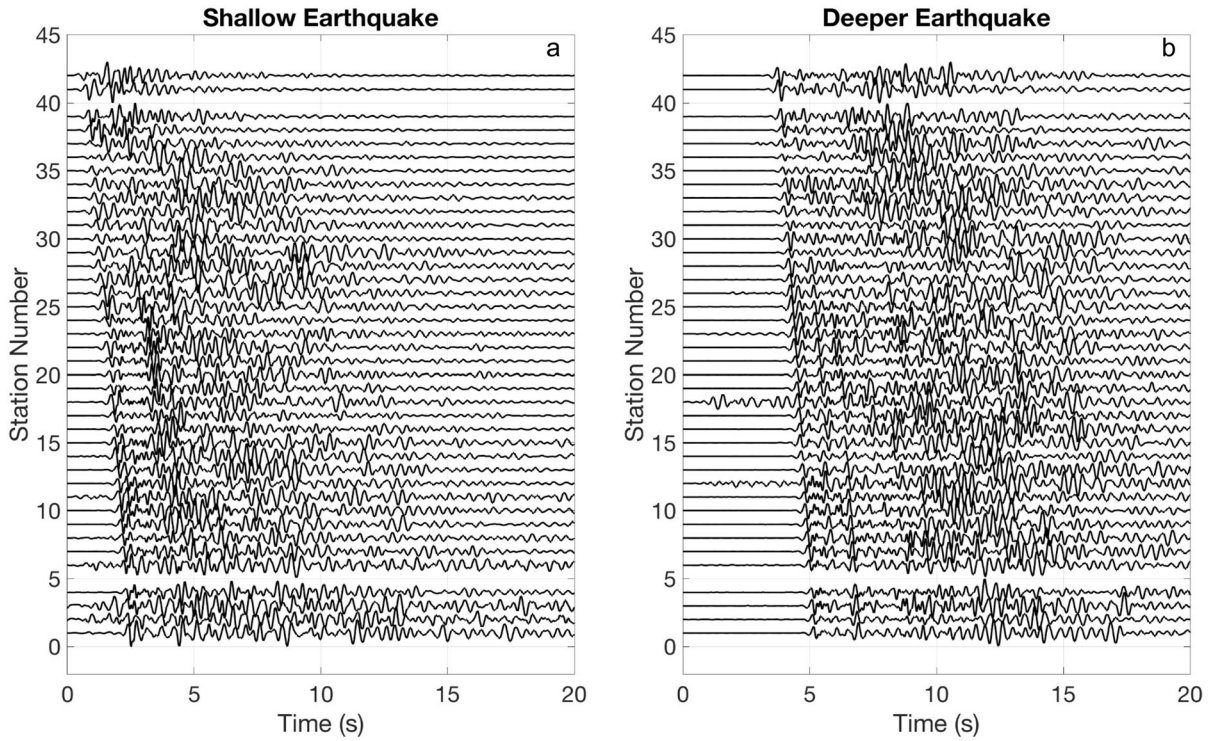

Figure 10
Seismic records of **a** shallow earthquake and **b** deeper earthquake from the line array along SAF (Line 3 in Fig. 9). The records are bandpass-filtered at 1–3 Hz and start at the origin times of the two earthqaukes from the USGS catalog. Station 1 is the farthest receiver from the two earthquakes

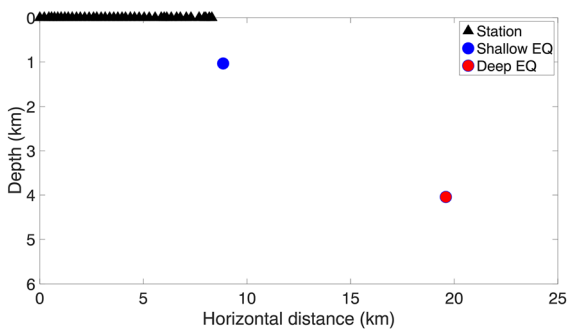

Figure 11
Cross-section of the selected earthquakes and seismic array along the SAF

stationary phase zone of the two earthquakes, we can reconstruct the same waveforms using the records from the L3 array and the full line surface array. By contrast, varying the depth of the shallow earthquake, we can retrieve the similar waveforms but with different phases of the direct arrivals (red and blue dashed lines on Fig. 13b. The depth uncertainty only affects the phase shift of the waveforms but does not reshape the waveform.

Since we verified that the depth uncertainty of the selected earthquakes does not affect the shape of the retrieved waveform, we speculate that the recovered later arrival after approximately 3 s is a guided wave traveling inside the low-velocity fault zone of the SAF. To investigate whether the fault-zone wave guide qualitatively produces the observed waveform characteristics, we simulate the wave propagation between a source and a receiver in a 3-layer model, both of which are located in the middle slow-velocity layer. This is a crude model (Fig. 14) for the host rock and the slow-velocity layers of the SAF (Li et al. 2004; Jeppson and Tobin 2015). The elastic model is the plan view of the SAF and accounts for P-S wave conversions. We use a source-time function given by a Ricker wavelet with the dominant frequency at 3.3 Hz. Assuming the two earthquakes

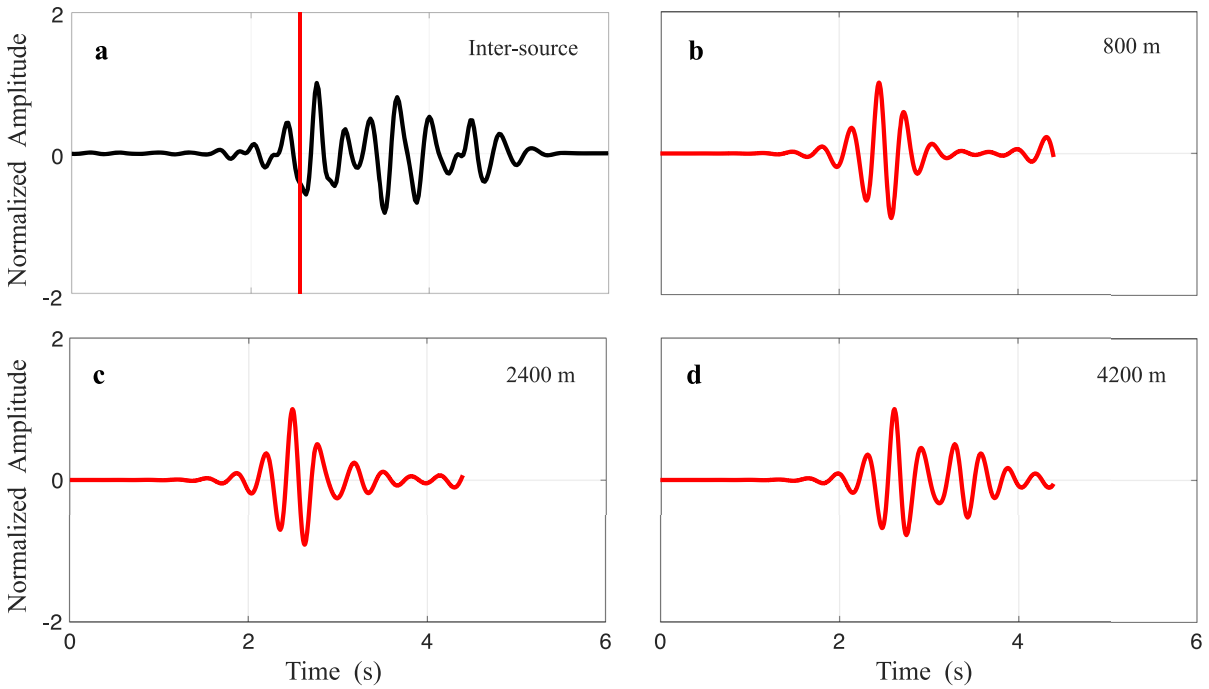

Figure 12

a Inter-source interferometry of 1–3 Hz bandpass-filtered P-waves. Vertical red line indicates the expected arrival time of the direct P waves determined from the earthquake catalog and the local P-wave velocity. Numerical simulations of wave propagation in a 3-layer model between a source and a receiver with a thickness of the low-velocity layer of **b** 800 m, **c** 2.4 km, and **d** 4.2 km

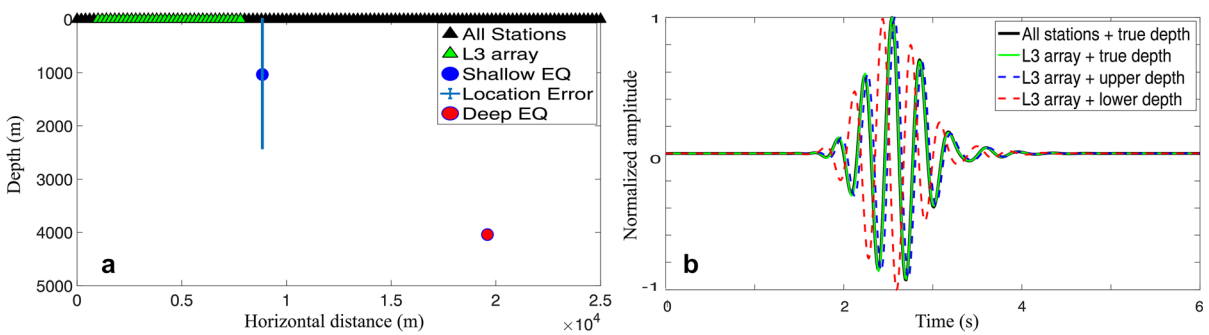

Figure 13

a Synthetic model to compute acoustic wavefields. The model includes surface receivers with receiver spacing of 200 m and two sources located at the same depth of the selected earthquakes from the SAF. The errorbar indicates the depth uncertainty of the shallow earthquake from the earthquake catalog. The green receivers indicate the location of Line 3 (L3) array along the SAF in Fig. 9. **b** The inter-source interferometric waveforms reconstructed using all surface receivers and the true depth of the shallow earthquake (solid black), L3 receiver and the true depth of the shallow earthquake (solid green), L3 receiver and the shallow earthquake located at the surface (dashed blue), L3 receiver and the shallow earthquake located at the lower end of the errorbar in a (dashed red)

occurred inside the fault zone of the SAF, we model the source and receiver inside the low-velocity zone with horizontal and vertical separation distance of 12 km and 350 m, respectively (Fig. 14). The horizontal distance of 12 km is approximately the same separation distance between the two earthquakes (Fig. 11). The vertical distance of 350 m is arbitrarily chosen to be less than the smallest fault-zone

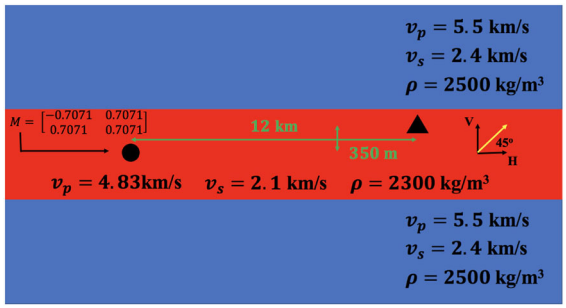

Figure 14
Numerical model of 3 layers used to simulate 2D wave propagation between a source and a receiver in a low-velocity layer (red) The yellow arrow indicates the direction in which the wave motion is recorded

thickness of the SAF, which is less than 1 km (Li et al. 1990, 2004; Korneev et al. 2004; Holdsworth et al. 2011; Zoback et al. 2011; Jeppson and Tobin 2015). This arbitrarily chosen vertical distance also minimizes reflection interference effects from the two boundaries of the slow-velocity layers in our 3-layer model (Fig. 14). We simulated the wavefield with a 2D spectral element method (Tromp et al. 2008) for low-velocity layers with a thickness from 700 m to 7 km. The 2D simulation cannot be expected to quantitatively explain the waveforms; it is a crude model to explain the qualitative features of the extracted waveforms.

Examples of the wavefield with the middle layer thickness of 800 m, 2.4 km, and 4.2 km, respectively, are shown in Fig. 12; the wavefields are bandpass-filtered between 2.5 Hz and 3.8 Hz to account for the dominant frequency of the interferometric signal at approximately 3.2 Hz. The modeled seismograms (Fig. 12b, c, d) illustrate that a low-velocity zone with a thickness of 4 km best explains the qualitative features of the extended wavetrains obtained from inter-source interferometry (Fig. 12a). Figure 12 suggests that the later arrival is likely to consist of guided waves travelling in the damage zone of SAF with a thickness of approximately 4 km. The crude model used cannot be expected to lead to a fit of the synthetic waveforms with the waves extracted with the VRM, but the qualitative similarity between the wavefields estimated by the interferometry and the numerical simulation illustrates that inter-source interferometry can qualitatively estimate the wavefield, which accounts for the wave propagation between two earthquake sources.

5. Discussion

Body waves contain three pieces of information: 1) the arrival time of the direct wave, 2) the waveform of the direct wave, and 3) the waveform of the coda wave. Using inter-source interferometry, one can reconstruct the direct wave and the coda of a body wave that propagates between two seismic sources, but the retrieved arrival time of the direct body wave may not be accurate.

The retrieved arrival time depends on the difference between the origin time of the two sources, which comes from the earthquake catalog. Using inter-source interferometry, one cross-correlates earthquake seismograms with start time at the origins as recorded in the event catalog. However, the origin time information taken from the catalog cannot be assumed to be precise, and errors in the origin time lead to errors in the arrival time of the extracted direct wave. In addition, the depth uncertainty of the selected two earthquake and the limited aperture of used seismic array also contribute to the phase shift of the retrieved waveform (Sects. 3, 4, Fig. 13, and the Appendix) and thus maps the phase error to the errors in the arrival time retrieval.

We can reconstruct the waveform of the direct body wave by using receivers located within the stationary phase zone of the two sources. Retrieving this waveform offers a variety of benefits. For example, by selecting two earthquakes occurring in a fault or subduction zone, and using the inter-source technique, we can reconstruct the waveform of the direct body wave that travels along the zones and is influenced by the structure of these zones (Fig. 15); the direct wave travels in the low-velocity zone of the fault zone or subduction zone. This direct wave helps to define properties such as the width (thickness) and the wave velocity of the zones, for example by using fault-zone guided wave as a diagnostic of structure of fault zones (Li et al. 1990).

Using VRM, one needs an adequate sampling density of receivers to reconstruct waveforms of direct body waves. In practice, if the waves propagate

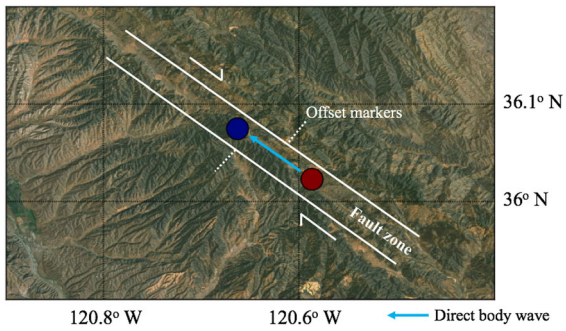

Figure 15
Cartoon of the map view of the fault-zone-guided waves that travels in a fault zone of the SAF. The shown fault zone width is not to scale. The cartoon is the plan view of the numerical model in Fig. 14

horizontally along surface receivers, one needs adequate sampling points of 4 samples/wavelength to directly integrate the interferometric wavefield (Fan and Snieder 2009). However, additional processes prior to the integration of oscillatory functions such as interpolation and Filon-Trapezoidal rule (Entwistle et al. 2015; Tuck 1967) can reduce the sampling requirements and one only needs more than 2 sampling points in a wavelength to adequately sample the interferometric wavefields. This sampling density can be larger if the wave arrives at an angle to the receivers because only the wavelength along the surface contributes to the wave reconstruction; the required receiver spacing changes to $\lambda/sin(i)$, where λ and i denote the wavelength and the incident angle of the wavefront to the receiver array, respectively.

As Eq. (1) illustrates, to recover the waveform of coda waves using inter-source interferometry, one needs receivers on a closed surface surrounding the sources. Because the dominant contribution of Green's function retrieval comes from the receivers located inside stationary phase zones, one can reconstruct scattered waves using surface receivers only if scatterers are located below seismic events (Fig. 16a). However, one needs underground receivers rather than surface receivers to recover the waveform of coda waves if scatterers are located above the events (Fig. 16b). Although Fig. 16 shows a sketch with a scatterer, one can apply similar reasoning when retrieving coda waves from a reflector (e.g., core-mantle boundary and Moho discontinuity).

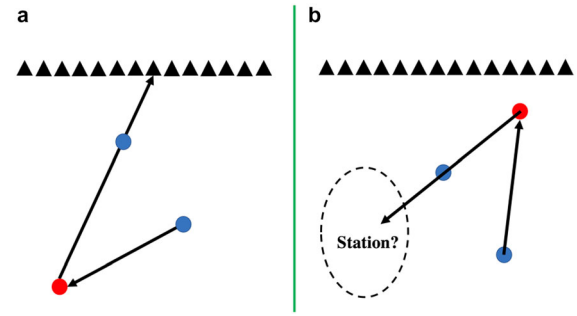

Figure 16
Cartoon of receiver locations needed for the retrieval of coda waves. **a** and **b** have a scatterer (red) located below and above two seismic events (blue)

Our synthetic examples show that to retrieve the waveform of direct body waves, one needs to use surface receivers located in the stationary phase zone of the selected sources with enough sampling density. These limitations apply to any advances of inter-source interferometry. Curtis and Halliday (2010) apply inter-source interferometry as an operation for source-receiver interferometry, which estimates the Green's function accounted for the wave propagation between a virtual source and a vitual receiver. The operation requires the stationary phase zone to be parallel to the virtual source and a set of sources located on the closed surfaces surrounding the virtual

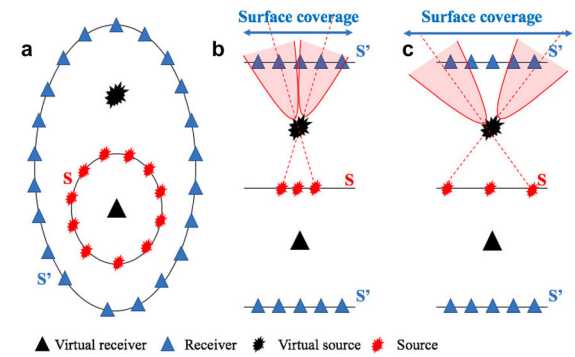

Figure 17
Different geometries of source-receiver interferometry, modified from Fig. 5 in Curtis and Halliday (2010). **a** source-receiver geometry with two closed surfaces: S surrounding a virtual receiver and S' surrounding a virtual source. **b** source-receiver geometry with limited surface receiver coverage controlled by the stationary phase zones of sources on the surface S and the virtual source. **c** similar source-receiver geometry to **b** but with more sparsely distributed sources on the surface S, leading to a larger surface receiver coverage. Pink hyperbolae denote the stationary phase zones

receiver (Fig. 17). Thus, the geometry of the sources and the virtual source control the size and the location of the stationary phase zone and the surface receiver coverage. Depending on the distribution of the sources, we may need a large aperture for the stationary phase zone and the surface coverage, or we may need the entire surface array if the set of sources are very sparsely distributed away from the virtual source (Fig. 17c). The requirement for surface receiver coverage also applies to other interferometric advances. For example, in the virtual source method application, the surface coverage controls the geometry of the target area and source-receiver positions as well as the resolution of the reconstructed wavefields (Bakulin and Calvert 2006).

In Sect. 4, we illustrate a field example of inter-source interferometry of P waves recorded from two earthquakes in the SAF area, in which the recorded seismograms of the example satisfy the stationary phase location and sampling criteria. Because we lack seismic wavefields across the SAF and only use seismograms from the array along the fault (Line 3, Fig. 9) for the inter-source method, we can only qualitatively reconstruct the P wavefield accounting for the wave propagation between the two earthquakes. The retrieved wavefield and the wave simulation using a 2D fault model suggest that the damage zone of the SAF is approximately 4 km thick. The thickness inferred from the interferometric waveform is different than the thickness of the SAF damage or fault zone that is estimated to be less than 1 km, in previous studies of the nearby areas of the SAF (Li et al. 1990, 2004; Korneev et al. 2004; Holdsworth et al. 2011; Zoback et al. 2011; Jeppson and Tobin 2015). The difference in the thickness estimates may be from the diversity of our investigated seismic frequency of 1-3 Hz compared to the other studies. Korneev et al. (2004) investigate the fault zone guide wave of the SAF areas at approximately 3-8 Hz while the investigated trap waves of Li et al. (1990) contain frequency contents approximately below 100 Hz. Although Li et al. (2004) study trapped waves with a frequency content below 5 Hz (similar frequency content to our study), the investigated guided waves are part of the S coda which is different to our investigated P coda. Thus, the difference in the frequency content and the wave types considered may explain the difference of the estimated thickness of the SAF damage zone. Other explanations for our different estimates for the thickness may be found in the following studies of nearby SAF areas and other strike slip faults: 1) the shallow structure of the SAF may contain local flower structures and splay faults that expand approximately up to 1-3 km (Unsworth et al. 1997; Delong et al. 2010) and 2) off-fault deformations may occur and extend up to 1-2 km away from the primary rupture zone (Zinke et al. 2014; Vallage et al. 2015; Gold et al. 2015). In addition, the 1-3 Hz bandpass-filtered wavefield of the selected deeper earthquake recorded at receivers across the SAF (Line 1 and 2, Fig. 9) illustrates a high energy and complicated waveforms in a band with a width of approximately 4 km across the SAF (Fig. 18), supporting the thickness determined by the interferometric wavefield.

In our SAF example, we used the inline receivers only and only have receivers with a limited aperture. As a result, we can only recover the qualitative waveform but do not retrieve the complete waveform of the P wavefield. Halliday and Curtis (2008) show that using an in-line array for interferometry of surface waves induces phase shifts compared to the true Green's function. Seismic interferometry implicitly involves integration of oscillatory integrals where the dominant contribution comes from the stationary phase point. According to expression (24.40) of Snieder and van Wijk (2015), each stationary phase integral gives a phase contribution $\exp(\pm i\pi/4)$, where the sign is determined by the curvature of the phase function. Leaving out the stationary phase integration in the transverse direction gives a phase error of $\pm\pi/4$. Since we only seek to compare the character of the waveforms qualitatively, this phase error is not significant.

Our work shows that inter-event interferometry of two earthquakes cannot recover the complete waveform of coda waves but can retrieve the waveform of the direct body waves, and the accuracy of the retrieved arrival time of the direct waves depends on the accuracy of the earthquake catalog. The lack of transverse receiver array also contributes to the incomplete recovery of the direct body waves. However, in active-source explorations, particularly on land, one has a well-defined catalog of the

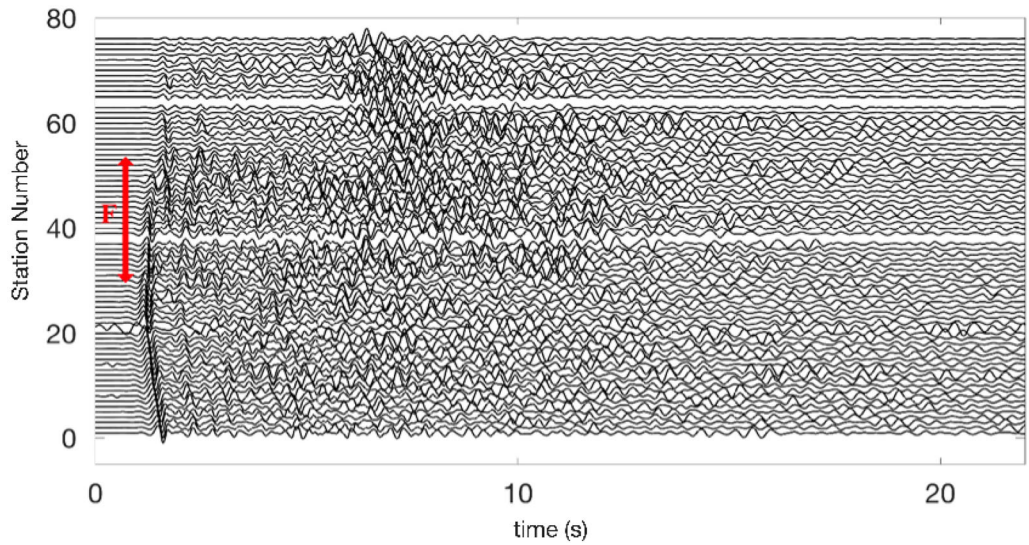

Figure 18
Seismograms with 1–3 Hz bandpass filter of the selected deeper earthquake in Fig. 11, recorded at receivers across the SAF (Line 1 and 2, Fig. 9). The red arrow shows the approximately wide region that straddles the SAF where the waveforms show an increase in complexity

locations and timing of active sources. Using inter-source interferometry and well-cataloged active sources, one can better recover the arrival time of the direct body waves with smaller timing errors, compared to the uses of global or local earthquakes.

6. Conclusion

Although one can reconstruct a body wave propagating between two seismic sources (e.g., earthquakes) using inter-source interferometry, the retrieved arrival time of the direct body wave depends on the difference between the origin times of the earthquakes that are extracted from the earthquake catalog, and parts of the catalog could be inaccurate. Moreover, we show that the depth uncertainty influences the phases of the retrieved direct arrival and maps the error to the retrieved arrival time. Thus, the retrieved arrival time may be useful only if the origin times and depths of the used events in the catalog are accurate. However, when one knows the source-time function of at least one of the sources (the virtual sensor), the waveforms of the direct and coda waves, which are part of the body wave propagated between the two sources, can be recovered using the inter-source method with receivers on a closed surface.

The retrieval of the waveforms of the direct and coda waves can also be approximated using surface receivers located in the associated stationary phase zones, but one can retrieve coda waves using surface receivers only if the waves are scattered and reflected below the shallowest source. Theoretically, one needs receivers in the stationary phase zone, which is a patch on the surface, to recover the direct or coda waves but in practice one may use receivers along a line array.

To reconstruct accurate body waves propagated between two sources using inter-source interferometry, one needs to satisfy two conditions: (1) using receivers inside the stationary phase location and (2) the sampling criteria of approximately 4 samples/wavelength for the direct summation of interferometric wavefields over receivers. In this paper, we illustrate an example of direct P-wave reconstruction using the inter-source method and real-earthquake wavefields from the SAF satisfying the two requirements. Using finite-element modelling and a simplified seismic velocity model for the SAF region with a slow-velocity fault zone embedded in a homogeneous medium, we test the effect of different

fault zone thicknesses on the waveform character. We find that a fault zone thickness of approximately 4 km is needed to qualitatively match the wavetrains of the P waves recovered using VRM. The width of the fault zone determined from the interferometric waveform and our modelled solution is consistent with the distance over high-energy, highly scattered, and complicated waveforms manifested on recordings from surface receivers across the fault.

Acknowledgements

We thank colleagues from Center for Wave Phenomena (CWP) for useful discussions, Robert Clayton (Caltech) for the seismic records used in this study, and Ridvan Orsvuran for helping with the 2D spectral element method modelling. The authors thank the editors from the journal of Pure and Applied Geophysics for handling this manuscript and thank Andrew Curtis for constructive and critical comments that helped to improve this work. P Saengduean is financially supported by DPST, the Development and Promotion of Science and Technology Talents Project (Royal Government of Thailand scholarship). The authors declare that they have no competing interests.

Appendix A: Phase Shift and Fresnel Integral

In Sect. 3, we show that one can reconstruct direct and scattered body waves using receivers in the stationary phase zones. Using an array with a limited aperture in the stationary phase region, the phase of the recovered waveforms differs slightly from the forward-modelled waveforms (Figs. 5, 6, and 7).

When we use the source-receiver geometry in Fig. 2, we can determine the time differences between the direct arrivals of the two sources at each receiver. We define the size of the stationary phase zone (SPZ) using a faction of the dominant period $T_{dominant}$ of our synthetic signals, where $T_{dominant} = 0.25$ s. In Sect. 3, our SPZ covers the receivers within $T_{dominant}/4$ from the maximum time difference (Fig. 19).

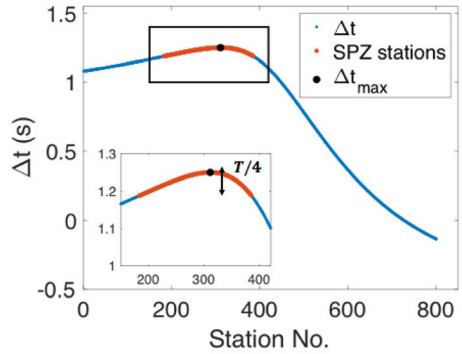

Figure 19
Time differences between the direct arrivals of the two sources at each surface receiver in Fig. 2. The graph on the bottom left corner is the enlarged version of the area inside the black box

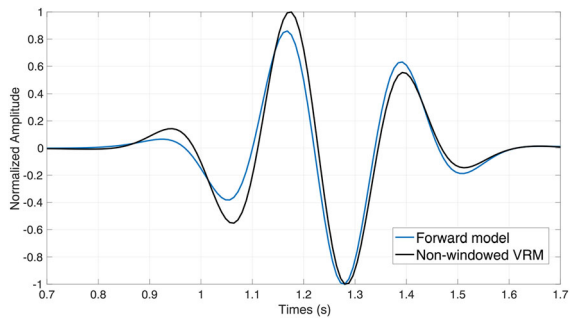

Figure 20
The forward-modeled and the interferometric waveforms of the direct body waves

Figure 20 shows the direct wave that propagates between the two sources in Fig. 2, and the waves extracted from inter-source interferometry take only receivers into account with a delay time $T_{dominant}/4$ relative to the delay time at the stationary phase zone. One should note the slight phase change between the two waveforms. We show in this appendix that this phase error is associated with limiting the used receivers to the stationary phase region.

Consider the source-receiver geometry in Fig. 21. Seismic interferometry for waves in a 2D homogeneous medium gives

$$G(r_A, r_B, \omega) - G^*(r_A, r_B, \omega) \approx \frac{i}{4\pi\rho} \oint_{S'} \sqrt{\frac{1}{r_{SA} r_{SB}}} e^{ik(r_{SA} - r_{SB})} dS', \tag{9}$$

where $G(r_A, r_B, \omega) - G^*(r_A, r_B, \omega)$ is the difference between the causal and acausal parts of the Green's

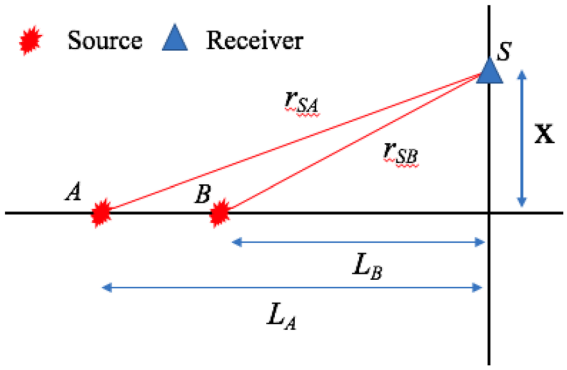

Figure 21
Source and receiver positions in interferometry. x is the half-width of the stationary phase zone

function accounting for the wave propagation between the points A and B, ω is the angular frequency, ρ is the mass density, k is the wave number, and S is the source position on a surface S' (Fan and Snieder 2009). We can approximate the term $r_{SA} - r_{SB}$ in Eq. (9) using a second-order Taylor series:

$$r_{SA} - r_{SB} \approx (L_A - L_B) + \frac{1}{2}\left(\frac{1}{2L_A} - \frac{1}{2L_B}\right)x^2. \quad (10)$$

Using this second order Tayor expansion for the phase and replacing the geometrical spreading in Eq. (9) by $1/\sqrt{L_A L_B}$, the integral in expression (9) is in the stationary phase approximation (Snieder and van Wijk 2015) given by

$$G(r_A, r_B, \omega) - G^*(r_A, r_B, \omega) \approx \frac{i}{4\pi\rho}\frac{e^{ik(L_A - L_B)}}{\sqrt{L_A L_B}}\int_{-\infty}^{+\infty}\exp\left(\frac{ik}{2}\left(\frac{1}{L_A} - \frac{1}{L_B}\right)x^2\right)dx\,, \quad (11)$$

where we replaced the integration over a closed surface by an integration over the transverse x-coordinate. The integral in the right-hand side is of the same form as the Fresnel integral (Sandoval-Hernandez et al. 2018), which is defined as

$$F(X) = \int_0^X \exp\left(i\frac{\pi}{2}x'^2\right)dx'\,. \quad (12)$$

This integral is complex and is shown in the complex plane in Fig. 22 where the the origin corresponds to the integral for $X = 0$, and the asymptotic point $0.5 + 0.5i$ is reached for $X \to \infty$. This graphical representation is called the *Cornu spiral*. The many windings

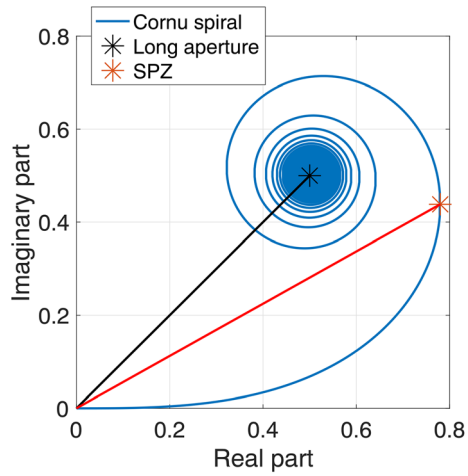

Figure 22
Fresnel integral from $t = 0$ to $t \to \infty$ in the complex domain (blue). Black and red asterisks represent the integral over a large part of surface receivers and surface receivers located in the stationary phase zone, respectively

of this spiral around the asymptotic point reflect that the Fresnel integral converges slowly.

The real part of the integrand of the Fresnel integral (12) is shown in Fig. 23. The oscillatory nature of this integrand explains the shape of the Cornu spiral and the slow convergence of the Fresnel integral: the alternating positive and negative values of the integrand lead to the slow spiraling of the Fresnel integral in the complex plane, and one needs

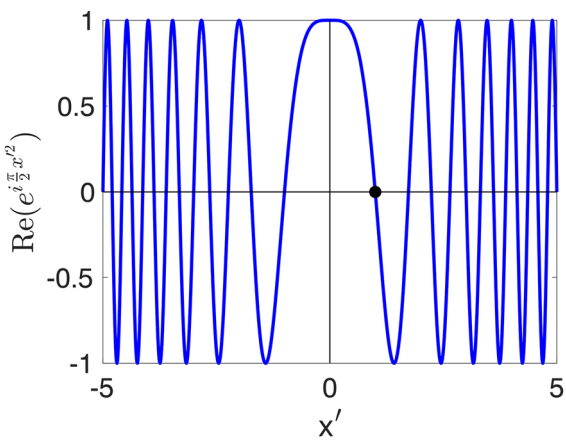

Figure 23
Real part of the integrand of the Fresnel integral (12) for $-5 < x' < 5$. Black dot denotes the first position where the real part changes from positive to negative values

to integrate over a large interval for the integral to be close to its asymptotic value for $X \rightarrow \infty$.

In the waveforms of Fig. 20 the summation over receivers was limited to receivers that have a delay time of less than a 1/4 of the dominant period. That corresponds to a phase delay of less than $\pi/2$. In the Fresnel integral (12), this integration interval corresponds to the upper limit $X = 1$. As shown by the black dot in Fig. 23, this upper limit is at the point where the real part of the Fresnel integral has its first zero crossing. (This is actually the rationale for restricting the integration to delay times less than 1/4 of the dominant period.) Since the real part of the integrand of the Fresnel integral changes sign, the real part of the Fresnel integral has a maximum at this point, and hence this upper limit corresponds to the rightmost point of the Cornu spiral that is indicated by the red star in Fig. 22.

The important point to note is that the phase of the Fresnel integral for $X = 1$ differs from the phase of the integral computed for its asymptotic value for $X \rightarrow \infty$; the phase angle for the red star in Fig. 22 differs by about 0.273 rad from the phase angle for the black star. This phase difference leads to the phase difference in the waveforms shown in Fig. 20. The phase difference in the waveforms corresponds to about 0.201 rad. This is slightly less than the phase difference of 0.273 rad predicted above. This discrepancy is caused by the fact that the argument in this appendix ignores the decay of the interferometric integral that is due to variations of the geometrical spreading in the integration. Furthermore, the analysis in this appendix is applicable in the frequency domain, whereas the time-domain waveforms in Fig. 20 contain contributions from a range of frequencies. However, the main points from this appendix are that (1) the interferometric integral converges slowly and (2) truncating this integral can leads to phase errors of about 0.3 rad. Tapering of the interferometric integral will lead to a faster convergence of the integral. Since the phase error does not depend on the distance between the sources at locations A and B, the impact of the phase error on estimated velocities decreases with increasing distance between the sources.

References

Aki, K., & Richards, P. (2002). *Quantitative seismology* (2nd ed.). Univ Science Books.

Asano, K., Iwata, T., Sekiguchi, H., Somei, K., Miyakoshi, K., Aoi, S., & Kunugi, T. (2017). Surface wave group velocity in the Osaka sedimentary basin, Japan, estimated using ambient noise cross-correlation functions. *Earth, Planets and Space, 69*(108), 1–20.

Bakulin, A., & Calvert, R. (2006). The virtual source method: Theory and case study. *Geophysics, 71*(4), SI139–SI150.

Burdick, L. J., & Orcutt, J. A. (1979). A comparison of the generalized ray and reflectivity methods of waveform synthesis. *Geophysical Journal of the Royal Astronomical Society, 58*(2), 261–278.

Curtis, A., Gerstoft, P., Sato, H., Snieder, R., & Wapenaar, K. (2006). Seismic interferometry—Turning noise into signal. *The Leading Edge, 25*(9), 1082–1092.

Curtis, A., & Halliday, D. (2010). Source-receiver wave field interferometry. *Physical Review E, 81*(4), 046601.

Curtis, A., Nicolson, H., Halliday, D., Trampert, J., & Baptie, B. (2009). Virtual seismometers in the subsurface of the Earth from seismic interferometry. *Nature Geoscience, 2*(10), 700–704.

Delong, S. B., Hilley, G. E., Rymer, M. J., & Prentice, C. (2010). Fault zone structure from topography: Signatures of en echelon fault slip at Mustang Ridge on the San Andreas Fault, Monterey County, California. *Tectonics, 29*(5), 1–16.

Draganov, D., Wapenaar, K., Mulder, W., Singer, J., & Verdel, A. (2007). Retrieval of reflections from seismic background-noise measurements. *Geophysical Research Letters, 34*(4), L04305.

Entwistle, E., Curtis, A., Galetti, E., Baptie, B., & Meles, G. (2015). Constructing new seismograms from old earthquakes: Retrospective seismology at multiple length scales. *Journal of Geophysical Research: Solid Earth, 120*(4), 2466–2490.

Eulenfeld, T. (2020). Towards source region tomography with inter-source interferometry: Shear wave velocity from 2018 West Bohemia swarm earthquakes. *Journal of Geophysical Research: Solid Earth [manuscript submitted for publication]*, pages 1–24.

Fan, Y., & Snieder, R. (2009). Required source distribution for interferometry of waves and diffusive fields. *Geophysical Journal International, 179*(2), 1232–1244.

Forghani, F., & Snieder, R. (2010). Underestimation of body waves and feasibility of surface-wave reconstruction by seismic interferometry. *The Leading Edge, 29*(7), 790–794.

Gold, R. D., Reitman, N. G., Briggs, R. W., Barnhart, W. D., Hayes, G. P., & Wilson, E. (2015). On- and off-fault deformation associated with the September 2013 Mw 7.7 Balochistan earthquake: Implications for geologic slip rate measurements. *Tectonophysics, 660,* 65–78.

Guy, M. R., Patton, J. M., Fee, J., Hearne, M., Martinez, E., Ketchum, D., et al. (2015). *National Earthquake Information Center systems overview and integration 2015–1120* (p. 25). U.S: Geological Survey Open-File Report.

Halliday, D., & Curtis, A. (2008). Seismic interferometry, surface waves and source distribution. *Geophysical Journal International, 175*(3), 1067–1087.

Holdsworth, R. E., van Diggelen, E. W., Spiers, C. J., de Bresser, J. H., Walker, R. J., & Bowen, L. (2011). Fault rocks from the SAFOD core samples: Implications for weakening at shallow depths along the San Andreas Fault, California. *Journal of Structural Geology, 33*(2), 132–144.

Jeppson, T. N., & Tobin, H. J. (2015). San Andreas fault zone velocity structure at SAFOD at core, log, and seismic scales. *Journal of Geophysical Research: Solid Earth, 120,* 4983–4997.

Korneev, V., Nadeau, R., & Berkeley, L. (2004). Vibroseis Monitoring of San Andreas Fault in California. *University of California, Lawrence Berkeley National Laboratory*, (https://escholarship.org/uc/item/2t35c4x6).

Larose, E., Margerin, L., Derode, A., van Tiggelen, B., Campillo, M., Shapiro, N., et al. (2006). Correlation of random wavefields: An interdisciplinary review. *Geophysics, 71*(4), SI11–SI21.

Li, Y. G., Leary, P., Aki, K., & Malin, P. (1990). Seismic trapped modes in the Oroville and San Andreas fault zones. *Science, 249*(4970), 763–766.

Li, Y. G., Vidale, J. E., & Cochran, E. S. (2004). Low-velocity damaged structure of the San Andreas Fault at Parkfield from fault zone trapped waves. *Geophysical Research Letters, 31*(12), 1–5.

Liu, Y., Draganov, D., Wapenaar, K., & Arntsen, B. (2016). Retrieving virtual reflection responses at drill-bit positions using seismic interferometry with drill-bit noise. *Geophysical Prospecting, 64*(2), 348–360.

Matzel, E., Morency, C., Rhode, A., Templeton, D., Pyle, M., & Ave, E. (2016). Virtual seismometers in geothermal systems: looking inside the microseismic cloud. *Proceedings, 41st Stanford Geothermal Workshop on Geothermal Reservoir Engineering*, pages 1–4.

Miyazawa, M., Snieder, R., & Venkataraman, A. (2008). Application of seismic interferometry to extract P- and S-wave propagation and observation of shear-wave splitting from noise data at Cold Lake, Alberta, Canada. *Geophysics, 73*(4), D35–D40.

Mordret, A., Jolly, A., Duputel, Z., & Fournier, N. (2010). Monitoring of phreatic eruptions using interferometry on retrieved cross-correlation function from ambient seismic noise: Results from Mt. Ruapehu, New Zealand. *Journal of Volcanology and Geothermal Research, 191*(1–2), 46–59.

Morency, C. & Matzel, E. (2017). SGP-TR-212: Virtual seismometers for induced seismicity monitoring and full moment tensor inversion. *Proceedings of 42nd Workshop on Geothermal Reservoir Engineering*, 5:1–5.

Nakata, N., Snieder, R., Kuroda, S., Ito, S., Aizawa, T., & Kunimi, T. (2013). Monitoring a building using deconvolution Interferometry. I: Earthquake-data analysis. *Bulletin of the Seismological Society of America, 103*(3), 1662–1678.

Nakata, N., Snieder, R., Tsuji, T., Larner, K., & Matsuoka, T. (2011). Shear wave imaging from traffic noise using seismic interferometry by cross-coherence. *Geophysics, 76*(6), SA97–SA106.

Pianese, G., Petrovic, B., Parolai, S., & Paolucci, R. (2018). Identification of the nonlinear seismic response of buildings by a combined Stockwell Transform and deconvolution interferometry approach. *Bulletin of Earthquake Engineering, 16*(7), 3103–3126.

Poliannikov, O. V., Rondenay, S., & Chen, L. (2012). Interferometric imaging of the underside of a subducting crust. *Geophysical Journal International, 189*(1), 681–690.

Prieto, G. A., Lawrence, J. F., & Beroza, G. C. (2009). Anelastic Earth structure from the coherency of the ambient seismic field. *Journal of Geophysical Research: Solid Earth, 114*(7), 1–15.

Sandoval-Hernandez, M., Vazquez-Leal, H., Hernandez-Martinez, L., Filobello-Nino, U. A., Jimenez-Fernandez, V. M., Herrera-May, A. L., et al. (2018). Approximation of Fresnel integrals with applications to diffraction problems. *Mathematical Problems in Engineering, 2018,* 1–13.

Schuster, G. T. (2009). *Seismic Interferometry*. Cambridge: Cambridge University Press.

Shapiro, N. M., Campillo, M., Stehly, L., & Ritzwoller, M. H. (2005). High-resolution surface-wave tomography from ambient seismic noise. *Science, 307*(5715), 1615–1618.

Shen, Z., & Zhan, Z. (2020). Metastable olivine wedge beneath the Japan sea imaged by seismic interferometry. *Geophysical Research Letters, 47*(6), 1–8.

Shirzad, T., Riahi, M. A., & Assumpção, M. S. (2019). Crustal structure of the collision-subduction zone in South of Iran using virtual seismometers. *Scientific Reports, 9*(1), 1–11.

Snieder, R. (2004). Extracting the Green's function from the correlation of coda waves: A derivation based on stationary phase. *Physical Review E, 69*(4), 046610.

Snieder, R., & Larose, E. (2013). Extracting Earth's elastic wave response from noise measurements. *Annual Review of Earth and Planetary Sciences, 41*(1), 183–206.

Snieder, R., Miyazawa, M., Slob, E., Vasconcelos, I., & Wapenaar, K. (2009). A comparison of strategies for seismic interferometry. *Surveys in Geophysics, 30*(4–5), 503–523.

Snieder, R., & van Wijk, K. (2015). *A Guided Tour of Mathematical Methods for the Physical Sciences* (3rd ed.). Cambridge: Cambridge University Press.

Snieder, R., Van Wijk, K., Haney, M., & Calvert, R. (2008). Cancellation of spurious arrivals in Green's function extraction and the generalized optical theorem. *Physical Review E Statistical, Nonlinear, and Soft Matter Physics, 78*(3), 036606.

Snieder, R., Wapenaar, K., & Wegler, U. (2007). Unified Green's function retrieval by cross-correlation; Connection with energy principles. *Physical Review E Statistical, Nonlinear, and Soft Matter Physics, 75*(3), 036103.

Tromp, J., Komatitsch, D., & Liu, Q. (2008). Spectral-element and adjoint methods in seismology. *Communications in Computational Physics, 3*(1), 1–32.

Tuck, E. O. (1967). A simple "Filon-Trapezoidal'' rule. *Mathematics of Computation, 21*(98), 239–241.

Unsworth, M. J., Malin, P. E., Egbert, G. D., & Booker, J. R. (1997). Internal structure of the San Andreas Fault at Parkfield, California. *Geology, 25*(4), 359–362.

Vallage, A., Klinger, Y., Grandin, R., Bhat, H. S., & Pierrot-Deseilligny, M. (2015). Inelastic surface deformation during the 2013 Mw 7.7 Balochistan, Pakistan, earthquake. *Geology, 43*(12), 1079–1082.

van Dalen, K. N., Mikesell, T. D., Ruigrok, E. N., & Wapenaar, K. (2015). Retrieving surface waves from ambient seismic noise using seismic interferometry by multidimensional deconvolution. *Journal of Geophysical Research: Solid Earth, 120*(2), 944–961.

Vasconcelos, I., & Snieder, R. (2008a). Interferometry by deconvolution, Part 1—Theory for acoustic waves and numerical examples. *Geophysics, 73*(3), S115–S128.

Vasconcelos, I., & Snieder, R. (2008b). Interferometry by deconvolution: Part 2—Theory for elastic waves and application to drill-bit seismic imaging. *Geophysics, 73*(3), S129–S141.

Wapenaar, K., Draganov, D., Snieder, R., Campman, X., & Verdel, A. (2010). Tutorial on seismic interferometry: Part 1—Basic principles and applications. *Geophysics, 75*(5), 195–209.

Wapenaar, K., & Fokkema, J. (2006). Green's function representations for seismic interferometry. *Geophysics, 71*(4), SI33–SI46.

Zinke, R., Hollingsworth, J., & Dolan, J. F. (2014). Surface slip and off-fault deformation patterns in the 2013 MW 7.7 Balochistan, Pakistan earthquake: Implications for controls on the distribution of near-surface coseismic slip. *Geochemistry, Geophysics, Geosystems, 15*(12), 5034–5050.

Zoback, M., Hickman, S., & Ellsworth, W. (2011). Scientific drilling into the San Andreas fault zone—An overview of SAFOD's first five years. *Scientific Drilling, 1,* 14–28.

(Received September 18, 2020, revised June 20, 2021, accepted June 29, 2021, Published online July 19, 2021)